

Benzene Sulfonate Modified ZnCr-LDH and Its Enhanced Adsorption Properties for Anionic Dyes

Jia Lin (✉ lj18814386655@163.com)

Henan Polytechnic University

Yude Zhang

Henan Polytechnic University

Qian Zhang

Henan Polytechnic University

Jinli Shang

Henan Polytechnic University

Fuyao Deng

Henan Polytechnic University

Research Article

Keywords: Layered double hydroxide, Benzene sulfonate modification, Adsorption, Methyl orange (MO), Congo red (CR), Orange OII (OII)

Posted Date: February 8th, 2021

DOI: <https://doi.org/10.21203/rs.3.rs-164231/v1>

License:   This work is licensed under a Creative Commons Attribution 4.0 International License.

[Read Full License](#)

1 **Benzene sulfonate modified ZnCr-LDH and its enhanced adsorption properties for anionic dyes**

2 Jia Lin¹, Yude Zhang^{*,1,2,3}, Qian Zhang^{*,1,2,3}, Jinli Shang¹, Fuyao Deng¹

3
4 *Corresponding author: Yude Zhang, zhangyude@hpu.edu.cn,+8613203990290; Qian Zhang,
5 qianzh@hpu.edu.cn,+8613523196309

6 1 School of Chemistry and Chemical Engineering, Henan Key Laboratory of Coal Green Conversion,
7 Henan Polytechnic University, Jiaozuo, 454000, China

8 2 Collaborative Innovation Center of Coal Work Safety of Henan Province, Jiaozuo, 454000, China

9 3 Wuxi Feile High-performance Materials Co. LTD, Wuxi, 214000, China

10
11 **Abstract**

12 A benzene sulfonate modified hydrotalcite (SO₃-LDH) was synthesized by a facile one-pot
13 hydrothermal technique, which can efficiently remove methyl orange (MO), Congo red (CR) and
14 orange II (OII) from aqueous solution. After modified by benzene sulfonate, the microstructure of
15 hydrotalcite changes obviously, from the cellular structure to the stacking structure formed by the
16 face-face contact of hydrotalcite nanosheets, which resulted in much more exchangeable nitrate ions to
17 remain in the interlayer space. The pre-insertion of benzene sulfonate as a pillar expanded the interlayer
18 gallery, which facilitated the pollutant anions (MO, CR and OII) into the interlayer of LDH in the
19 subsequent adsorption process. The maximum adsorption capacity of SO₃-LDH for MO, CR and OII
20 was 4200.8 mg/g, 1252.0 mg/g and 1670.6 mg/g respectively, which is approximately 1.86 times, 1.8
21 times and 2.32 times that of the pristine NO₃-LDH, respectively. The removal mechanism of anionic
22 dyes was determined as anion exchange between NO₃⁻ ions and dye molecules. The adsorption
23 behavior for MO and OII is multilayer adsorption, while the adsorption behavior for CR is monolayer
24 adsorption. The adsorption process mainly was controlled by the chemical bonding between the dye
25 molecules and adsorbent active sites. The benzene sulfonate modified LDH has a great potential to be
26 used as a high-efficient adsorbent to remove anionic dyes from aqueous solution.

27
28 **Keywords:** Layered double hydroxide; Benzene sulfonate modification; Adsorption; Methyl orange
29 (MO); Congo red (CR), Orange OII (OII).

31 **1 Introduction**

32 With the widespread application of dyes in textile, leather, papermaking and other chemical
33 industries, a large amount of polluted water containing poisonous and hardly-degradable organic dyes
34 is discharged (Tao et al. 2017). Undoubtedly, these dye wastewater will lead to serious environmental
35 issues such as color pollution, light penetration interference, damage aquatic organisms, even harm to
36 human health. Therefore the effective treatment of dyeing wastewater is one of the most serious
37 concerns of the current era. So far, many techniques have been used to treatment dyeing wastewater,
38 such as adsorption methods (Zheng et al. 2019), chemical methods (Liu et al. 2013), biological
39 degradation methods (Pakshirajan and Kheria 2012), photocatalytic oxidation methods (Dinari et al.
40 2016; Mohapatra and Parida 2012), flocculation precipitation methods (Morshedi et al. 2013),
41 membrane filtration methods (Liu et al. 2018), and the combined treatment of different methods (Ou et
42 al. 2015). In these methods, adsorption is a simple, effective and low-cost way to remove of dyeing
43 wastewater (Zheng et al. 2019). Various kinds of adsorbents have been used for dyeing wastewater
44 treatment, such as activated carbon (Maneerung et al. 2016), clay minerals (Zhang et al. 2019b),
45 polymeric resins, transition metal composite (Zheng et al. 2017) and nanocomposites (Zheng et al.
46 2019). However, the adsorption capacity is limited. Therefore, efficient adsorbents with high adsorption
47 capacity and fast adsorption rate are urgently needed.

48 As one kind of useful multi-functional materials, layered double hydroxides (LDH) based on a
49 brucite-like ($Mg(OH)_2$) structure have been widely used as adsorbents for the removal of anionic
50 contaminants from dyeing wastewater owing to their layered and uniformly distributed structure,
51 flexible self-assembly and efficient modification of chemical compositions, large surface area, high
52 porosity and controllability of layer interval and anionic exchangeability (Mahjoubi et al. 2018; Tao et

53 al. 2017). Usually, the exchangeable anions compensating the positive charge of the LDH interlayers
54 include NO_3^- , CO_3^{2-} , SO_4^{2-} and Cl^- . A kind of ultra-small NiAl-Cl-LDH displayed favorable removal
55 performance toward MO was reported (Jing et al. 2019), which showed 900.1 mg/g maximum
56 theoretical adsorption capacity at $\text{pH} = 7$ and 298 K. The anion nitrate in the interlayer of
57 MgAl- NO_3 -LDH can also be exchanged by methyl orange (MO), orange II (OII) and orange G (OG)
58 (Darmograi et al. 2015), and the corresponding maximum adsorption capacity were 1800.3 mg/g, 945.9
59 mg/g and 769.0 mg/g respectively. In a more classical case (Mahjoubi et al. 2018), ZnAl layered double
60 hydroxides intercalated with carbonate, nitrate, chloride and sulphate ions exhibited exceptional
61 maximum adsorption capacities of 1684.0, 2270.0, 2455.0 and 2758.0 mg/g for MO, respectively.
62 These precursors can be effectively exchange with anionic dyes in wastewater.

63 In addition, a large number of organic molecules can be incorporated into the interlayer space,
64 such as aliphatic and aromatic carboxylates, sulfonates, alkyl sulfate anions and organic dyes (Mandal
65 et al. 2009). The organo-modification could change the surface hydrophilicity into hydrophobic nature
66 to strengthen the removal of organic pollutants in aqueous solution by the similar dissolve mutually
67 theory (Taviot-Guého et al. 2018). Soft-template synthesis has become highly desirable in the process
68 of organo-modification for LDH. In Soft-template synthesis method, sulfonates and alkyl sulfate anions
69 as a soft template agent can intercalate into the LDH host structure via ion exchange with a specific
70 anion (e.g., NO_3^- , CO_3^{2-} , SO_4^{2-} , OH^- , Cl^-). The intercalated anionic surfactants will expand the base
71 spacing of LDH host structure, which facilitated the pollutant anions into the interlayer gallery of LDH.
72 Dodecyl sulfate anion (DS^-) intercalated magnesium iron layered double hydroxide (MgFe-DS-LDH)
73 was prepared by the co-precipitation method in the presence of SDS aqueous solution (X. Ruan et al.
74 2013), the adsorption capacity of the organic contaminants (naphthalene, nitrobenzene, acetophenone)

75 by MgFe-DS-LDH was much greater than that of the pristine MgFe-CO₃-LDH and MgFe-NO₃-LDH.
76 Recently, a hierarchical organic three-dimensional MgAl-SDS-LDH was also successfully synthesized
77 via a one-step hydrothermal strategy using sodium dodecyl sulfate (SDS) as a soft template agent
78 (Zhang et al. 2019a), which can efficiently remove MO with the maximum adsorption capacity of
79 377.9 mg/g. The organic modified hydrotalcite samples were potential sorbents for the abatement of
80 organic contaminants. In this work, a benzene sulfonate modified hydrotalcite (SO₃-LDH) was
81 synthesized by a facile one-pot hydrothermal technique using methyl orange as a soft template agent,
82 and then the products were used to remove MO, CR and OII from aqueous solutions. The
83 microstructure, adsorption isotherms, adsorption kinetics and adsorption mechanism of the material
84 were systematically investigated. We found that MO, CR and OII were removed by anion exchange.
85 The adsorption properties of modified hydrotalcite was significantly better than that of unmodified
86 hydrotalcite, and showed very high adsorption capacity for the anionic dyes of MO, CR and OII.

87 **2 Materials and methods**

88 **2.1 Materials**

89 All of the chemicals used in this study were of analytical grade. Zn(NO₃)₂·6H₂O, Cr(NO₃)₃·9H₂O,
90 NaOH, methyl orange (MO), congo red (CR) and orange OII (OII) were purchased from MACKLIN
91 (China). The distilled water was used in all experiments.

92 **2.2 Preparation of unmodified and modified hydrotalcite**

93 Unmodified hydrotalcite was prepared by one-pot hydrothermal method. A mixed salt solution
94 containing Zn(NO₃)₂·6H₂O (0.67M) and Cr(NO₃)₃·9H₂O (0.33M) was titrated with the solution of
95 sodium hydroxide (2.0 M) up to pH 10.0 at room temperature, and stirred vigorously for 30 minutes.
96 The suspension was hydrothermally treated at 65 °C for 12 h, then washed with distilled water for

97 several times until the pH was neutral, and dried at 65 °C for 12 h. The obtained product was named
98 NO₃-LDH.

99 Modified hydrotalcite was also synthesized via one-pot hydrothermal method at a constant
100 solution pH of 10. In detail, the modifier of methyl orange was dissolved in 50mL water and prepared
101 into a 60 mmol/L solution. Then, a mixed salt solution (50 mL) containing Zn(NO₃)₂·6H₂O (0.67 M)
102 and Cr(NO₃)₃·9H₂O (0.33 M), and a 2.0 M NaOH solution were simultaneously added into the
103 modifier solution, the pH was maintained at 10. The mixture solution poured into hydrothermal reactor
104 and aged at 65°C for 12 h, and then washed repeatedly with distilled water. Finally, it was dried at
105 65 °C for 12 h. The obtained product was named SO₃-LDH.

106 **2.3 Characterization of ZnCr-LDH**

107 Powder XRD diagrams were recorded on a X-ray diffractometer (X'pert³ Powder, PANalytical)
108 equipped with a Beta filter Nickel at a scanning rate of 5.166°/min. The applied radiation is Cu K α
109 from a long fine-focus Cu tube operating at 40 kV and 40 mA. The FTIR spectra of the samples were
110 recorded using potassium bromide pellet technique (0.5 wt.% sample) on a NICOLET VERTEX
111 70V-spectrometer at the condition of 40 scans and 4 cm⁻¹ resolution. The morphologies of samples
112 were investigated using a scanning electron microscope (S4800 LV) with the accelerating voltage of 50
113 kV.

114 **2.4 Adsorption experiments**

115 The adsorption studies were carried out by batch method, the adsorption experiments was
116 performed in a series of 250 mL beakers containing 0.01g adsorbent and 100 mL of the MO, CR or OII
117 solution at the desired concentration. The initial dye concentration from 100 to 1000 mg/L. The
118 solution pH was adjusted to 5 with 0.1M HCl or 0.1M NaOH solution. Stirred the suspension at room

119 temperature until adsorption equilibrium. After MO, OII or CR solution adsorbed by the SO₃-LDH
120 samples, it was respectively named as SO₃-LDH-MO, SO₃-LDH-OII or SO₃-LDH-CR. Similarly, After
121 MO, OII or CR solution adsorbed by the NO₃-LDH samples, it was respectively named as
122 NO₃-LDH-MO, NO₃-LDH-OII or NO₃-LDH-CR. Then, the suspensions were centrifuged at 4000 rpm
123 for 20 min. The supernatant concentration was determined using a PERSEE TU-1810 UV-vis
124 spectrometer. The MO, OII and CR removal performance was evaluated by calculating the adsorbed
125 capacity at equilibrium (Q_e , mg/g) and at any time (Q_t , mg/g), and is given as Eq. (1) and (2):

$$126 \quad Q_t = (C_0 - C_t) V / m \quad (1)$$

$$127 \quad Q_e = (C_0 - C_e) V / m \quad (2)$$

128 where C_0 (mg/L) corresponds to the dye initial concentration, C_e (mg/L) is the dye equilibrium
129 concentration, C_t (mg/L) is the dye concentration in the aqueous solution at any time t (min), V (L) is
130 the solution volume, and m (g) is the adsorbent mass.

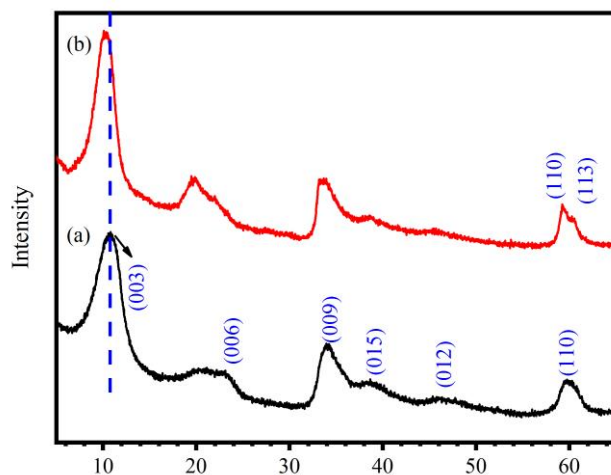
131 **3 Results and discussion**

132 **3.1 Characterization of materials**

133 **3.1.1 XRD analysis**

134 Fig.1 shows the XRD patterns of unmodified and modified hydrotalcite. The XRD pattern of
135 pristine NO₃-LDH is consisted of sharp and symmetrical diffraction peaks indicating good crystallinity
136 (Kloprogge et al. 2004; Kloprogge et al. 2005; Parida and Mohapatra 2012). The basal peaks for (003),
137 (006) and (009) crystal planes and non-basal peaks for the (015), (012) and (110) planes can be
138 observed from Fig. 1a. The (003) peak indicates the basal reflection of interlayer anion in LDH
139 materials. The interlayer distance of (003) basal plane (d_{003}) of the pristine NO₃-LDH is 8.269 Å. For
140 the modified sample (SO₃-LDH), the d_{003} value is 8.654 Å, and larger than that of NO₃-LDH, a new

141 peak appears at 19.698° , and the diffraction peak of (006) basal plane is absent, which indicates that
142 some benzene sulfonate anions enters the interlayer space of (003), (006) and (009) basal planes.



143
144

Fig.1. XRD patterns for the (a) $\text{NO}_3\text{-LDH}$ and (b) $\text{SO}_3\text{-LDH}$

145 3.1.2 FTIR analysis

146 Fig.2a shows the FTIR spectra of modifier. A broad peak at 3447 cm^{-1} is attributed to the
147 stretching mode of the OH bond of the hydroxyl groups and water molecules (Rojas Delgado et al.
148 2004). The position at 3180 cm^{-1} is associated with the peak of aromatic C–H stretch vibration in
149 modifier molecule. The position at 2808 cm^{-1} is the peak of aliphatic C–H stretching vibration
150 associated with CH_3 in modifier. A sharp aromatic C–C stretching band is observed at 1605 cm^{-1} . The
151 band at 1520 cm^{-1} is assigned to N=N. The peaks at 1365 and 1119 cm^{-1} are attributed to the C–N
152 bands (Zhang et al. 2019a) These peaks appear at 1421 cm^{-1} , 1165 cm^{-1} and 1036 cm^{-1} , which
153 originate from the stretching and vibrational mode of S=O in the sulfonate group ($-\text{SO}_3^-$). The peak at
154 1007 cm^{-1} is related to the in-plane bending vibration of C–H, and the rest peaks are ascribed to the
155 out-of-plane bending bands of C–H in aromatic nucleus.

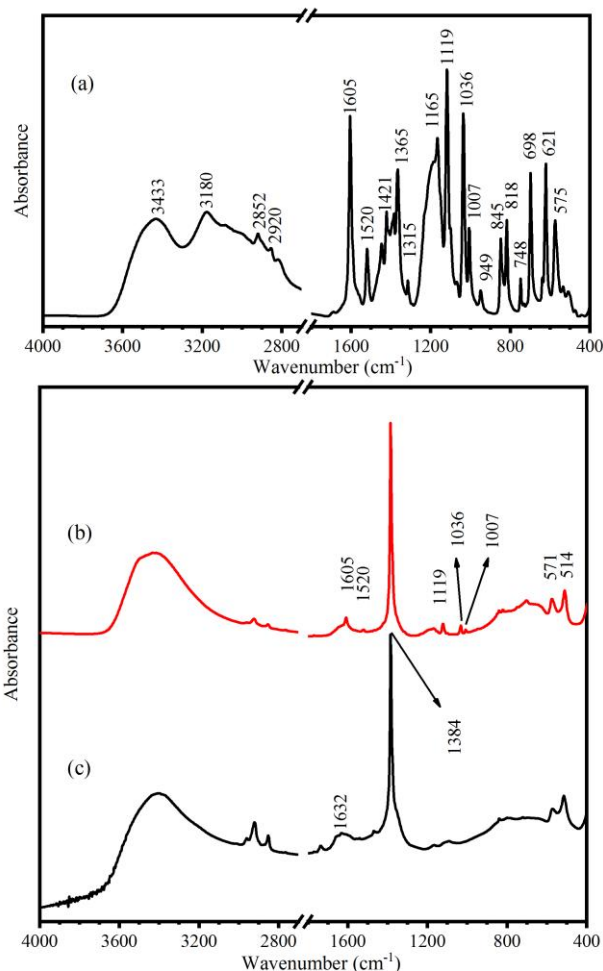


Fig.2. FT-IR spectra for (a) Modifier, (b) SO₃-LDH and (c) NO₃-LDH

156

157

158 Fig.2b and 2c shows the FTIR spectra of modified and unmodified samples. The FTIR spectra of

159 NO₃-LDH revealed the characteristic bands of hydroxalcite-like compounds. The broad and strong band

160 centered at 3400 cm⁻¹ is attributed to the stretching mode of the OH bond of the hydroxyl groups and

161 H₂O molecules. The weak band at 1632 cm⁻¹ is assigned to the bending vibration of the interlayer water,

162 and disappeared in the sample of SO₃-LDH. It shows that the hydrophobicity of hydroxalcite is

163 enhanced after modification. The strong absorption peak at 1384 cm⁻¹ is attributed to the antisymmetric

164 stretching mode of the NO₃⁻ anion. The bands below 1000 cm⁻¹ are due to M-O deformations and

165 translational bands. The band at 831 cm⁻¹ Zn-OH is out of plane bending mode. The band at 789 cm⁻¹ is

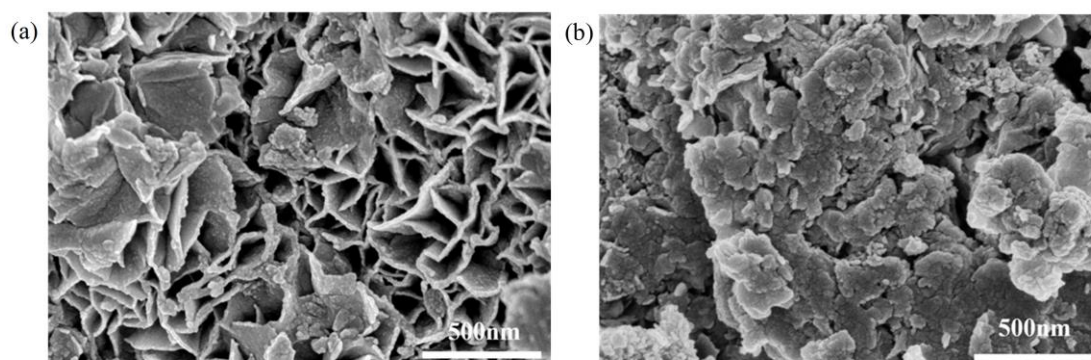
166 assigned to the Cr-OH deformation mode, and the bands at 571 cm⁻¹ and 514 cm⁻¹ are ascribed to the

167 Cr-OH translation.

168 The modification of hydrotalcite by benzene sulfonate anions is also confirmed by the FTIR
169 spectra. The aromatic C–C stretching band is observed at 1605 cm^{-1} . The bands at 1520 cm^{-1} is
170 assigned to N=N. The peak at 1119 cm^{-1} is attributed to the C–N bands. Stretching and vibrational
171 bands of the sulfonate group ($-\text{SO}_3^-$) are observed at 1421 cm^{-1} , 1165 cm^{-1} and 1036 cm^{-1} , and the
172 band of in-plane bending vibration of C–H is observed at 1007 cm^{-1} . For modified hydrotalcite, the
173 bands attributed to benzene sulfonate an including C–H, aromatic C–C, C–N, N=N and SO_3^- were
174 evident in the spectra, proving the benzene sulfonate anions of the modifier intercalation into the
175 interlayer of LDH.

176 3.1.3 SEM analysis

177 SEM image of the pristine NO_3 -LDH (Fig.3a) indicates a cellular structure assembled by the
178 side-face contacted ultra-fine LDH nanosheets (Costa et al. 2009). The thickness of LDH nanosheets is
179 about 20nm. For SO_3 -LDH (Fig.3b), the cellular structure basically disappears, and the LDH nanosheets
180 are packed together via face-face contact. Therefore, there are more sandwich structures formed by the
181 stacking of LDH nanosheets via face-face contact, which causes much more nitrate ions to remain in
182 the interlayer space, and further improves the anion exchange capacity of SO_3 -LDH.



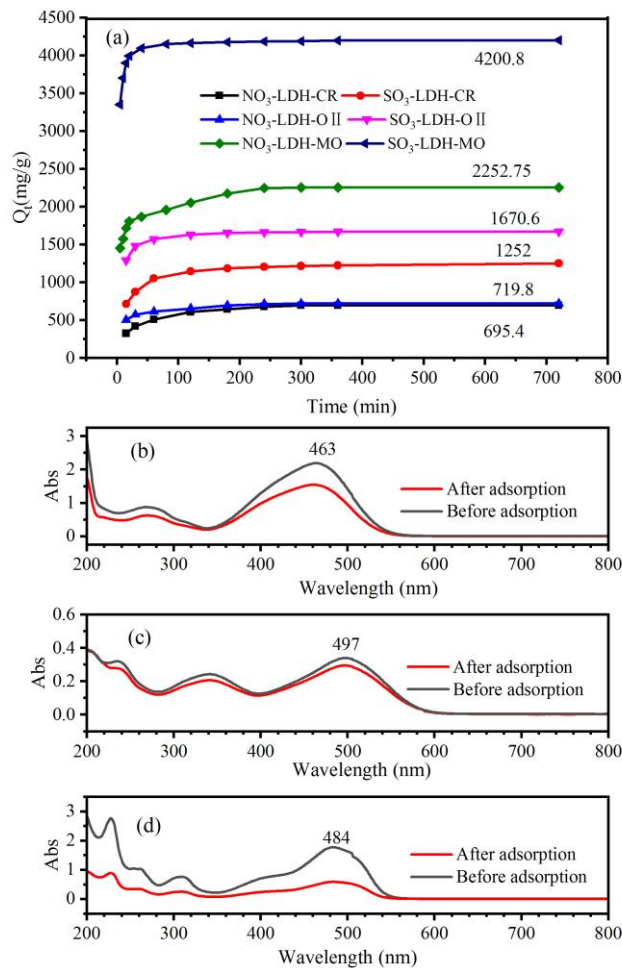
183

184 **Fig.3.** SEM images of (a) NO_3 -LDH and (b) SO_3 -LDH

185 3.2 Adsorption performance of unmodified and modified samples

186 In order to compare the adsorption performance of unmodified and modified LDH for different

187 dyes. The 10 mg adsorbent was dispersed in 100 mL MO, OII and CR solutions with an initial
 188 concentration of 1000 mg/L. The pH was adjusted to 5, stirred the suspension at room temperature. The
 189 adsorption capacity of NO₃-LDH and SO₃-LDH for dyes are shown in Fig.4a. The maximum
 190 adsorption capacity of MO by SO₃-LDH was about 4200.8 mg/g, and significantly higher than that of
 191 NO₃-LDH (2252.8 mg/g). The maximum adsorption capacity of CR and OII by SO₃-LDH was about
 192 1252.0 mg/g and 1670.6 mg/g respectively, and higher than that of NO₃-LDH (695.4 mg/g and 719.8
 193 mg/g). Therefore, SO₃-LDH has better adsorption performance for MO, CR and OII dyes.



194
 195 **Fig.4.** Adsorption of dyes by NO₃-LDHs and SO₃-LDH (a) ; Spectral scanning curve of (b) MO, (c) CR
 196 and (d) OII before and after SO₃-LDH adsorption

197 In addition, the stability of the SO₃-LDH as adsorption material was also studied. The three dye
 198 solutions before and after adsorbed by SO₃-LDH were diluted 20 times, respectively, and then

199 spectroscopically scanned by UV-vis spectrophotometer. As can be seen from Fig.4b, after SO₃-LDH
200 adsorbed MO, the intensity of characteristic peak of methyl orange was significantly reduced.
201 Obviously, SO₃-LDH can efficiently adsorb methyl orange in aqueous solution. Similarly, we can see
202 from Fig.4 c and Fig.4 d, the intensity of CR and OII characteristic peak was also reduced after
203 adsorbed by SO₃-LDH, but the location and number of the peak were not changed. Therefore, during
204 the adsorption process, the dye molecules intercalation into the interlayer of LDH will not be
205 exchanged into aqueous solution. It shows that the interlaminar sulfonate groups (–SO₃[–]) are confined
206 in the two-dimensional interlayer space by electrostatic interactions and/or hydrogen bonds with the
207 host layer, and are not readily to be exchanged by the anions of other dyes (Mandal et al. 2009).

208 3.3 Adsorption kinetics

209 To further investigate the adsorption rate of the three anionic pollutants by the SO₃-LDH sample.
210 the adsorption kinetics data was respectively analyzed by Pseudo-first-order and Pseudo-second-order
211 kinetic models (Zhang et al. 2019a), as the following equation Eq. (3) and (4):

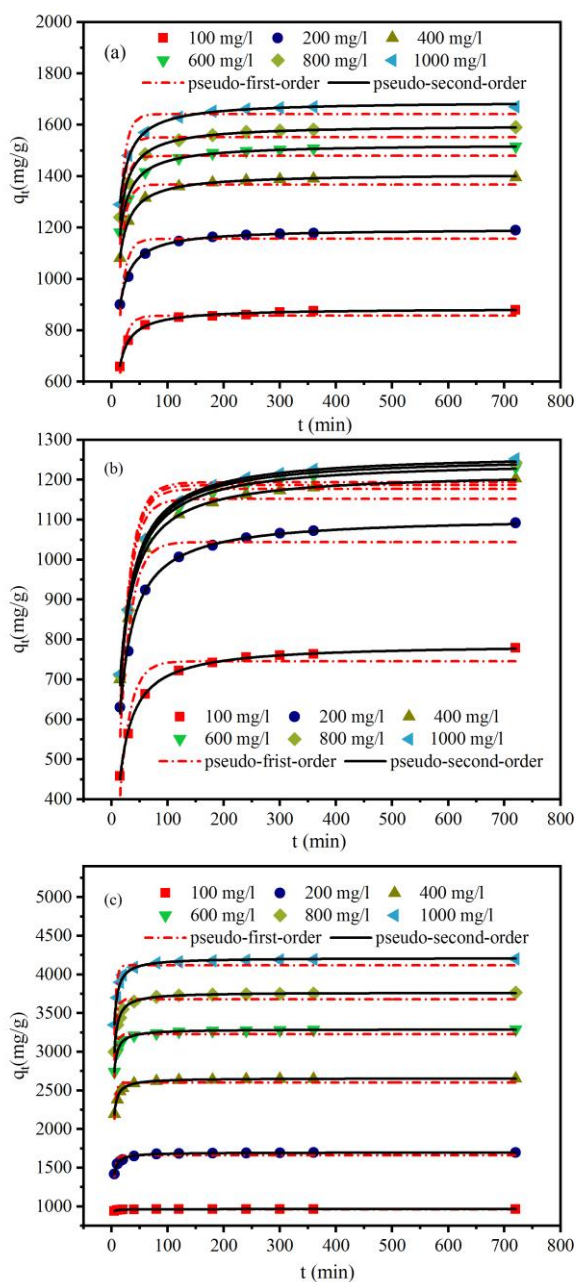
212 The pseudo-first-order: $q_t = q_e [1 - \exp(-K_1 t)]$ (3)

213 The pseudo-second-order: $q_t = K_2 q_e^2 t / (1 + q_e K_2 t)$ (4)

214 Where k_1 (min⁻¹) and k_2 (g/mg/min) are the rate constant of two models.

215 Fig. 5 displays the adsorption kinetic curves of SO₃-LDH for OII, CR and MO. All the kinetic
216 curves show that the adsorption rate is high in the initial phase, then gradually slows down, and finally
217 reaches equilibrium. With the increase of dyes concentration, the k_2 value is obviously reduced. The
218 change of K_2 values suggests that dyes concentration has a great influence on the adsorption rate. Some
219 experimental data are deviated from the fitting curve for the pseudo-first-order kinetic model, while
220 almost all the experimental data are distributed on the fitted curve for the pseudo-second-order kinetic
221 model. The corresponding parameters as shown in table 1, the R² values of the all curves fitted by the

222 pseudo-second-order kinetic model are closer to 1 compared with the curve fitted by pseudo-first-order
 223 kinetic model. Furthermore, the $Q_{e,cal}$ values for the pseudo-second-order model are closer to the
 224 experimental values ($Q_{e,exp}$). Therefore, the pseudo-second-order kinetic model is more suitable to
 225 explain the adsorption kinetics of these pollutants, the adsorption rate of SO_3 -LDH on three dyes is
 226 mainly controlled by the chemical bonding between the dye molecules and adsorbent active sites.



227
 228 **Fig. 5.** Fitted plots of the pseudo-first-order and pseudo-second-order kinetic models for (a) OII, (b) CR
 229 and (c) MO adsorption by SO_3 -LDH

230

231 **Table 1** Parameters in the two kinetic models for OII, CR and MO adsorption by SO₃-LDH

Pollutants	Concentration /(mg/L)	q _{e,exp} /(mg/g)	Pseudo-First-order model			Pseudo-second-order model		
			q _{e,cal} /(mg/g)	k ₁ /min ⁻¹	R ²	q _{e,cal} /(mg/g)	k ₂ /(mg/g ² min)	R ²
OII	100	878.8	856.7	0.09038	0.9003	884.7	0.000223	0.9974
	200	1189.6	1156.0	0.09085	0.8467	1195.0	0.000164	0.9967
	400	1395.5	1367.8	0.09660	0.8892	1409.0	0.000157	0.9993
	600	1516.0	1479.2	0.09745	0.8406	1524.9	0.000145	0.9970
	800	1591.2	1551.5	0.09785	0.8382	1599.3	0.000139	0.9968
	1000	1670.6	1641.6	0.09624	0.8979	1691.3	0.000130	0.9975
CR	100	778.6	745.7	0.05332	0.9154	788.8	0.000113	0.9984
	200	1092.0	1044.1	0.05083	0.9142	1106.9	0.000075	0.9968
	400	1203.0	1151.8	0.05169	0.9178	1219.5	0.000070	0.9963
	600	1231.0	1176.9	0.05039	0.9183	1248.1	0.000066	0.9967
	800	1242.8	1186.6	0.05027	0.9170	1258.8	0.000065	0.9971
	1000	1252.0	1193.5	0.04993	0.9149	1266.6	0.000064	0.9968
MO	100	964.5	961.4	0.74524	0.7019	964.8	0.007360	0.9959
	200	1698.8	1663.8	0.36132	0.7557	1697.1	0.000600	0.9964
	400	2654.0	2603.1	0.34295	0.7787	2656.8	0.000350	0.9976
	600	3290.0	3228.0	0.35421	0.7979	3290.9	0.000300	0.9986
	800	3766.0	3680.5	0.30957	0.7919	3767.4	0.000210	0.9980
	1000	4200.8	4118.9	0.30506	0.8150	4213.7	0.000180	0.9958

232 **3.4 Adsorption isotherms**

233 Equilibrium data, generally known as sorption isotherms are elementary necessity to comprehend
 234 the mechanism of the sorption [25]. There are a number of isotherm models such as Langmuir isotherm
 235 model, Freundlich isotherm model, Temkin isotherm model and the Dubinin–Radushkevich isotherm
 236 model (Liu and Wang 2021; Maneerung et al. 2016). The Langmuir monolayer adsorption and
 237 Freundlich multilayer adsorption models are commonly applicable to solid-liquid adsorption systems
 238 (Kausar et al. 2018; Tao et al. 2017).

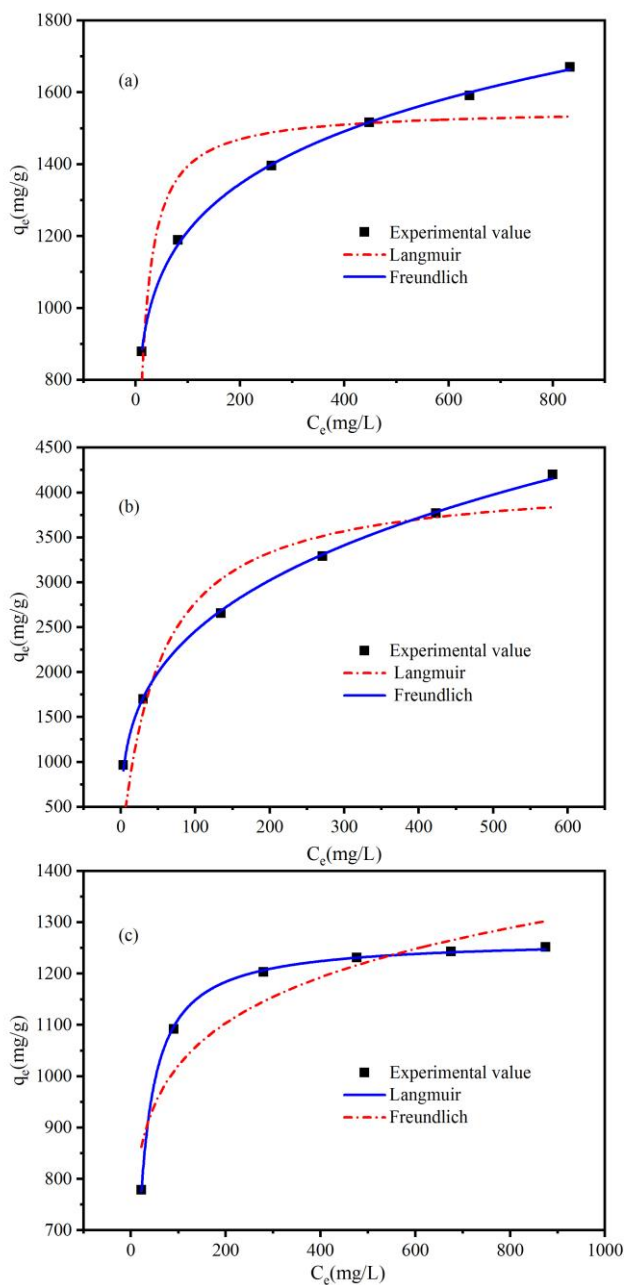


Fig. 6. Isotherm model for (a) OII, (b) MO and (c) CR adsorption on SO₃-LDH

Table 2 Parameters of isotherm model for OII, MO and CR adsorption on SO₃-LDH

Isotherm model	Pollutants	Parameters
Langmuir		$q_m(\text{mg/g})$ $K_L(\text{L/mg})$ R^2
	OII	1553.6 0.08785 0.8442
	MO	4169.5 0.01986 0.8932
	CR	1267.1 0.07130 0.9995
Freundlich		$K_F(\text{mg/g})(\text{mg/L})^n$ $1/n$ R^2
	OII	610.96 0.14897 0.9991
	MO	619.38 0.29917 0.9990
	CR	609.32 0.11212 0.8798

242 Fig. 6 displays the Langmuir and Freundlich isotherm curves for the OII, CR and MO adsorbed by
243 SO₃-LDH. The corresponding adsorption models (Zhang et al. 2019a) are expressed as follows Eq. (5)
244 and (6):

245 Langmuir: $q_e = k_L q_m C_e / (1 + K_L C_e)$ (5)

246 Freundlich: $q_e = k_F C_e^{1/n}$ (6)

247 Where Q_m is the maximum adsorption capacity of adsorbents (mg/g). K_L is the Langmuir
248 adsorption equilibrium constant (L/mg), which is related to the affinity of the binding site of the
249 adsorbent, the larger the value, the stronger the adsorption capacity. K_F is the Freundlich adsorption
250 equilibrium constant ((mg/g) (mg/L)ⁿ), which is related to the adsorption affinity, and n reflects the
251 supporting force of the adsorption process. If the empirical constant 1/n is between 0.1 and 0.5, it
252 means easy adsorption. If n=1, it is linear adsorption; If 1/n is greater than 2, adsorption is difficult to
253 occur.

254 The adsorption isotherms of SO₃-LDH for OII, MO and CR are shown in Fig. 6. As shown in
255 table 2, for OII and MO, the correlation coefficients (R²) for the Langmuir isotherm respectively are
256 0.8442 and 0.8932, while the R² values for the Freundlich isotherm respectively are 0.9991 and 0.9990.
257 Thus, Freundlich isotherm model is better to predict the OII and MO adsorption process. The
258 Freundlich assumed that the adsorption occurs on heterogeneous surfaces with non-uniform adsorption
259 sites. The K_F value respectively are 610.96 and 619.37, which suggests MO and OII have good
260 adsorption affinity with the surface of the adsorbent. The value of 1/n are 0.14897 and 0.29917 within
261 the range of 0.1–0.5, which indicates a favorable supporting force of the adsorption for OII and MO
262 adsorption by SO₃-LDH. The results shows that the adsorption of OII and MO by SO₃-LDH is
263 relatively easy to happen and belongs to multi-layer adsorption with strong adsorption affinity (Kausar

264 et al. 2018). For CR, the R^2 for the Langmuir isotherm is larger than the Freundlich isotherm models.
 265 Langmuir isotherm model greatly predicted the CR adsorption process, the adsorption occurs on a
 266 homogeneous adsorbent surface and belongs to single-layer adsorption.

267 **Table 3** Comparison of adsorption capacities of various adsorbents for dyes

pollutants	Adsorbents	pH	Temperature (°C)	Adsorption isotherm	q_m (mg/g)	References
MO	SO ₃ -LDH	5	25	Freundlich	4200.8	In this work
	MgAl-LDH	3-11	25	Freundlich	377.9	(Zhang et al. 2019a)
	SNiFe-LDH	3	25	Freundlich	387.6	(Zubair et al. 2018)
	NiFe-Cl-LDH	5-6	30	Langmuir	769.2	(Gao et al. 2018)
	ZnMgAl-LDH	3.0	25	Freundlich	883.2	(Zheng et al. 2012)
	ZnAl-Cl-LDH@Al(OH) ₃	4.5	25	Langmuir	1013.5	(Guo et al. 2018)
	MgAl-Cl-LDH	-	25	Langmuir	1112.0	(Xu et al. 2017)
	Co ₄ Fe-NO ₃ -LDH	7.1-7.3	25	Langmuir	1290.0	(Ling et al. 2016)
	ZnAl-CO ₃ -LDH	3.5-4.5	-	Langmuir	1684.0	(Mahjoubi et al. 2018)
ZnAl-NO ₃ -LDH	3.5-4.5	-	Langmuir	2270.0	(Mahjoubi et al. 2018)	
CR	ZnAl-Cl-LDH	3.5-4.5	-	Langmuir	2455.0	(Mahjoubi et al. 2018)
	ZnAl-SO ₄ -LDH	3.5-4.5	-	Langmuir	2758.0	(Mahjoubi et al. 2018)
	SO ₃ -LDH	5	25	Langmuir	1252.0	In this work
	Mg ₄ Al-LDH/CF	-	25	Langmuir	271.0	(Sun and Chen 2020)
	ZnFe ₂ O ₄ /MgAl-LDH	-	25	Langmuir	294.1	(Sun et al. 2020)
	ZnAl-LDH	3	-	Freundlich	591.8	(El Khanchaoui et al.)
	ZIF-ZnAl-LDH	-	45	Langmuir	909.1	(Li et al. 2020)
	Ni/Mg/Al-LDH	7	30	Langmuir	1250.0	(Lei et al. 2017)
O II	SO ₃ -LDH	5	25	Freundlich	1670.6	In this work
	Calcined MgAl-LDH	-	-	Langmuir	602.0	(Yan et al. 2016)
	LDH/PEG	-	50	Langmuir	724.6	(Mandal et al. 2019)
	Mg ₂ Al-NO ₃ -LDH	7	40	Langmuir	1265.0	(Mustapha Bouhent et al. 2011)
	HTMacro-cal	7	25	Langmuir	1521.2	(Géraud et al. 2007)
	NiAlTi-LDH	8	25	Langmuir	2000.0	(Rathee et al. 2020)

268 In order to position the adsorption performance of SO₃-LDH, Comparison of the adsorption
 269 capacity of this work and that of LDH material reported in literature is shown in table 3. The results
 270 show that the experimental Q_m of SO₃-LDH in this work is significantly superior to all of the reported
 271 LDHs containing different interlayer anions, and shows very high adsorption capacity. In general, the

272 as-synthesized $\text{SO}_3\text{-LDH}$ is a promising adsorbent for the removal of anions from dye containing
273 effluents.

274 **3.5 Adsorption mechanism**

275 **3.5.1 XRD analysis**

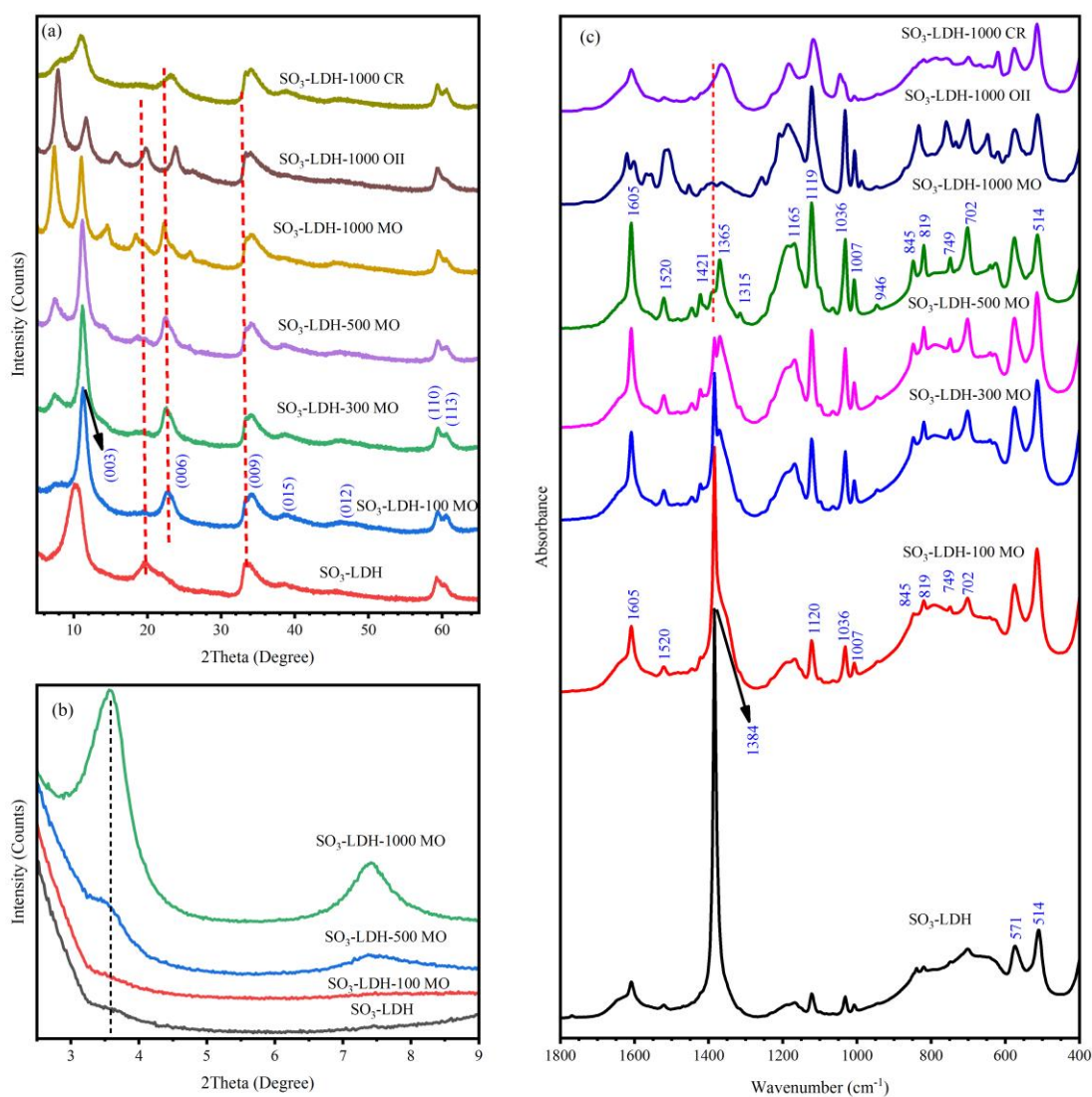
276 XRD patterns of different dyes adsorbed by $\text{SO}_3\text{-LDH}$ are shown in Fig. 7a and Fig. 7b. The d_{003}
277 value is 8.654 Å for the sample of $\text{SO}_3\text{-LDH}$. After $\text{SO}_3\text{-LDH}$ adsorbed by MO solutions of different
278 concentration, the (003), (006) and (009) diffraction peaks all shift to the lower angles. As the
279 increasing concentration of MO solution, the position offset of (003) reflection gradually decrease
280 along with much larger d_{003} value of 7.849 Å, 7.9045 Å, 7.923 Å and 7.998 Å for the samples of
281 $\text{SO}_3\text{-LDH-100MO}$, $\text{SO}_3\text{-LDH-300MO}$, $\text{SO}_3\text{-LDH-500MO}$ and $\text{SO}_3\text{-LDH-1000MO}$, and the intensities
282 of (003) reflection gradually weakens. Meanwhile, four new peaks are observed at the position of 7.40°,
283 14.62°, 18.36° and 25.76° related to the intercalation of (006), (009) (015) and (012) basal reflection
284 (Darmograi et al. 2015; Zhang et al. 2019a) as shown in Fig.7a, and a new strong peak appeared at 2θ
285 positions of 3.56° corresponding to d-values of 24.78 Å attributed to the intercalation of (003) basal
286 reflection by MO^- anions in the low angle XRD patterns of Fig.7b, and its intensities progressively
287 enhance, which indicates more and more MO^- anions are inserted into the interlayers of hydrotalcite
288 host with the increasing concentration of MO solution. For the sample of $\text{SO}_3\text{-LDH}$ adsorbed by the
289 1000mg/L OII solution ($\text{SO}_3\text{-LDH-1000OII}$), the profiles of all diffraction peaks are similar to that of
290 the $\text{SO}_3\text{-LDH-1000MO}$ sample except the positions are close to the higher angle, and sulfonate anions
291 of OII also inserted into the interlayers of (006) parallel crystal plane in LDH host structure, the
292 intercalated peak of (006) basal plane is located at 7.901°, and the corresponding interlayer distance
293 (d_{006}) is about 11.180 Å. After the $\text{SO}_3\text{-LDH}$ adsorbed by 1000 mg/L CR solution ($\text{SO}_3\text{-LDH-1000CR}$),

294 the peak intensities of (003) and (006) basal reflection reduce, along with a new weak peak ascribed to
295 the intercalated peak of (006) basal plane appeared at the position of 8.13° , and the corresponding d_{006}
296 value is about 10.863 \AA , which indicates sulfonate anions of CR also entered into the interlayer of (006)
297 parallel crystal plane.

298 **3.5.2 FTIR analysis**

299 FTIR spectroscopy was conducted to investigate the interaction between the $\text{SO}_3\text{-LDH}$ and the
300 dye molecules. In order to identify the adsorption mechanisms, the FTIR spectra of $\text{SO}_3\text{-LDH}$ adsorbed
301 by different dyes are shown in Fig.7c. As the increasing MO solution concentration from 100mg/L to
302 1000mg/L , the intensities of the adsorption bands at 1605 cm^{-1} ascribed to aromatic C–C stretching
303 vibration, at 1520 cm^{-1} assigned to N=N bands, at 1365 and 1119 cm^{-1} attributed to the C–N bands, at
304 1421cm^{-1} , 1165 cm^{-1} and 1036 cm^{-1} related to the stretching vibrational mode of S=O in the sulfonate
305 group ($-\text{SO}_3^-$), at 1007 cm^{-1} related to the in-plane bending vibration of C–H, and at 946 cm^{-1} ,
306 845 cm^{-1} , 819 cm^{-1} , 749 cm^{-1} and 702 cm^{-1} ascribed to the out-of-plane bending of C–H in aromatic
307 nucleus are remarkably enhanced. The strong peak around 1384 cm^{-1} attributed to the antisymmetric
308 stretching mode of the NO_3^- anion (Kloprogge et al. 2005) are gradually weakened. The decrease of the
309 NO_3^- anions is related to the increase of MO molecules intercalated into the interlayer and absorbed on
310 the surface of $\text{SO}_3\text{-LDH}$ sheets. The increasing sulfonate along with decreasing nitrate shows that ion
311 exchange becomes more intense in the interlayers of $\text{SO}_3\text{-LDH}$ with the increase of MO solution
312 concentration. For the samples of $\text{SO}_3\text{-LDH}$ adsorbed by the 1000mg/L OII ($\text{SO}_3\text{-LDH-1000 OII}$) and
313 1000mg/L CR solution ($\text{SO}_3\text{-LDH-1000 OII}$), the intensities of all the adsorption bands of aromatic
314 C–C, N=N and C–N bands, S=O stretching vibration and the in-plane and the out-of-plane bending
315 vibration of C–H in aromatic nucleus are significantly increased, and the intensity of the adsorption

316 band of the antisymmetric stretching mode of the NO_3^- anion is dramatically decreased, which suggests
 317 that there is an obvious ion exchange between NO_3^- anion and sulfonate group ($-\text{SO}_3^-$). Therefore, the
 318 adsorption of OII, CR and MO is achieved through the ions exchange with the NO_3^- ions of the
 319 $\text{SO}_3\text{-LDH}$.

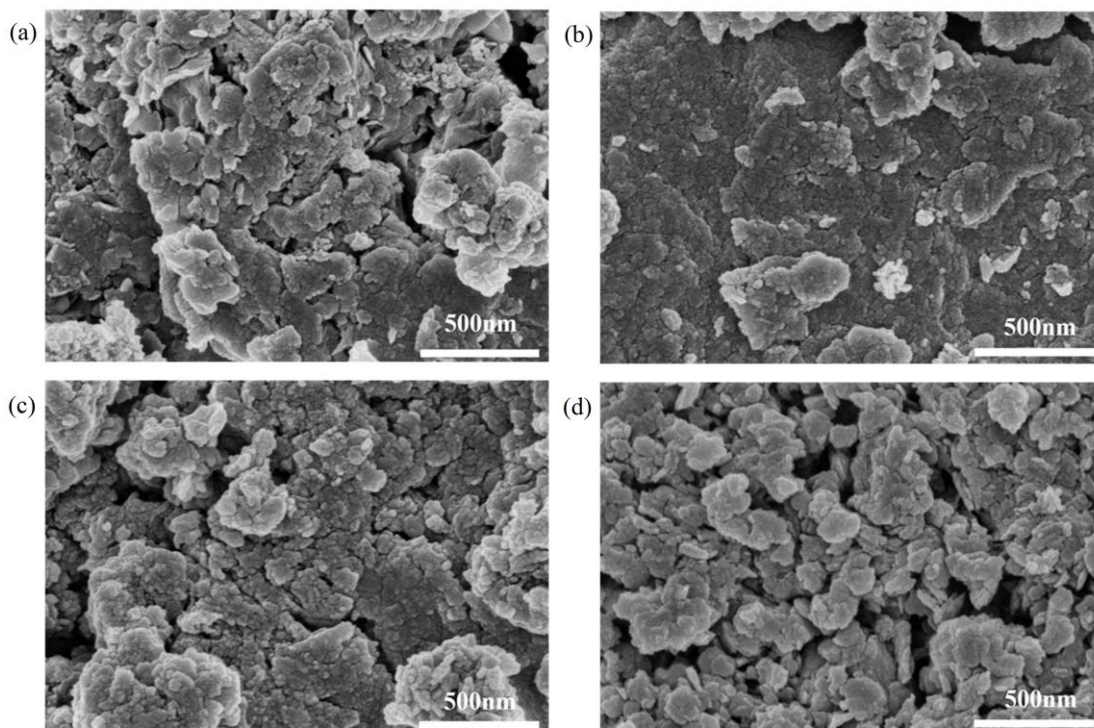


320
 321 **Fig. 7.** The XRD patterns (a, b) and FTIR spectra (c) of different dyes adsorbed by $\text{SO}_3\text{-LDH}$

322 **3.5.3 SEM analysis**

323 SEM images of $\text{SO}_3\text{-LDH}$ before and after adsorbed by MO are shown in Fig.8. After the
 324 $\text{SO}_3\text{-LDH}$ adsorbed 100mg/L MO solution, the nanosheets of $\text{SO}_3\text{-LDH-100}$ become much tighter and
 325 larger (Fig.8b). After the $\text{SO}_3\text{-LDH}$ adsorbed more MO^- anions, the LDH sheets in the sample of

326 $\text{SO}_3\text{-LDH-500}$ becomes loose (Fig.8c), and that of $\text{SO}_3\text{-LDH-1000}$ become much looser and smaller
327 (Fig.8d).

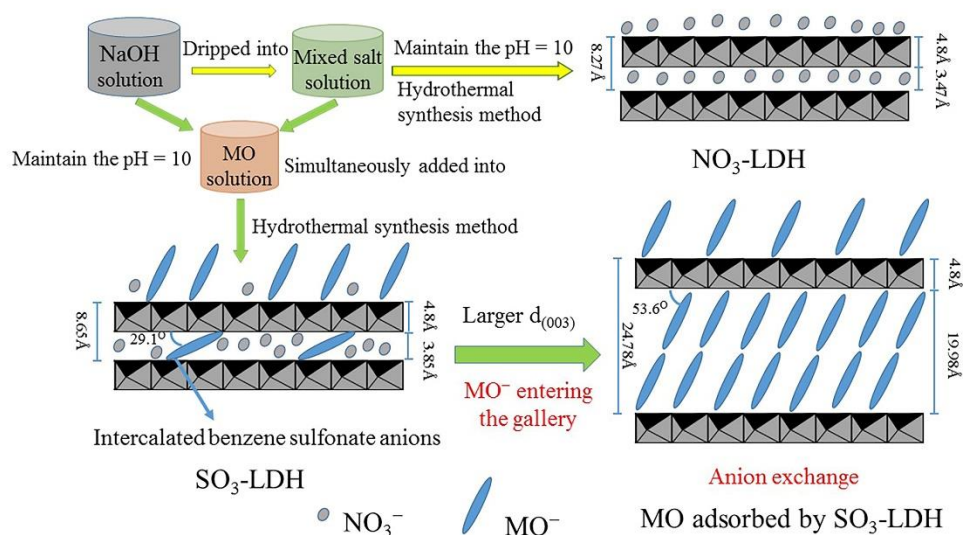


328
329 **Fig. 8.** SEM images of $\text{SO}_3\text{-LDH}$ before and after adsorbed different concentrations MO solutions: (a)
330 0 mg/L, (b) 100 mg/L, (c) 500 mg/L and (d) 1000 mg/L

331 3.5.4 Schematic illustration

332 The schematic illustration of the synthetic process of benzene sulfonate modified and unmodified
333 hydrotalcites by one-pot hydrothermal method and the adsorption process of MO by $\text{SO}_3\text{-LDH}$ were
334 shown in Fig.9. Modified hydrotalcite ($\text{SO}_3\text{-LDH}$) was prepared using methyl orange as a soft template
335 agent. Compared with unmodified hydrotalcite ($\text{NO}_3\text{-LDH}$), the insertion of benzene sulfonate anions
336 into the hydrotalcite layer resulted in the increase of the interlayer Spacing from 8.269 Å to 8.654Å.
337 The LDH host structure pre-intercalated by benzene sulfonate anions evolved into pillared layered
338 materials, benzene sulfonate anions as a column expanded the interlayer spacing of (003) base plane,
339 which facilitated the pollutant anions (MO, CR and OII) into the interlayer of $\text{SO}_3\text{-LDH}$ and exchanged
340 with NO_3^- anion in the subsequent adsorption process. Theoretically, the dimension of MO^- is

341 approximately 1.3 nm (Ling et al. 2016), and the thickness of one LDH sheet is about 0.48 nm. It is
 342 easily calculated that a basal spacing of 1.78 nm and 3.08 nm would be observed for monolayer and
 343 bilayer models (Xu et al. 2017) with perpendicular orientation of the MO in the interlayer space of
 344 LDH. We can infer that a small amount of benzene sulfonate anions pre-inserted into the gallery of
 345 hydrotalcite with a monolayer model in the process of hydrotalcite modification, and its inclination
 346 angle is calculated to be about 29.1°. After the SO₃-LDH sample adsorbed MO molecules, dye
 347 molecules intercalated again into the LDH host and successful exchange with NO₃⁻ anions (Darmograi
 348 et al. 2015), the d₀₀₃ value increased to 24.78 Å. A large amount of MO⁻ anions were intercalated into
 349 the gallery of SO₃-LDH with a bilayer model according to the Freundlich isotherm model, the tilting
 350 angle increases to 53.6°. The adsorption capacity of MO by SO₃-LDH was significantly enhanced to
 351 4200.8 mg/g, which was much higher than that of NO₃-LDH (2252.8 mg/g).



352
 353 **Fig.9.** Schematic illustration of the synthetic process of LDH materials and adsorption process of MO
 354 by SO₃-LDH

355 **4 Conclusions**

356 A benzene sulfonate modified ZnCr-layered double hydroxide (SO₃-LDH) was fabricated via a

357 facile one-pot hydrothermal technique. The pre-intercalated benzene sulfonate anions as the pillars
358 expanded the interlayer gallery, which facilitated the pollutant anions (MO, CR and OII) into the
359 interlayer of LDH in the subsequent adsorption process. The SO₃-LDH with good crystallinity
360 exhibited super high adsorption capacity of 4200.8 mg/g, 1252.0 mg/g and 1670.6 mg/g for MO, CR
361 and OII, much larger than NO₃-LDH. Therefore benzene sulfonate modification can greatly improve
362 the adsorption property of hydrotalcite. The adsorption of the three dyes on the SO₃-LDH followed
363 pseudo second-order kinetic model. The adsorption of OII and MO fitted the Freundlich adsorption
364 isotherm model, while Langmuir isotherm model greatly predicted the CR adsorption process. The
365 removal of these three dyes mainly depends on anionic exchange. SO₃-LDH has the advantages of fast
366 adsorption rate and high adsorption capability, and can be used as a potential adsorbent for anionic dye
367 wastewater.

368 **Authors' contributions** JL: investigation, formal analysis, writing and editing, conduct experiment;
369 YZ: conceptualization, methodology, supervision, writing and editing; QZ: funding acquisition; JS:
370 conduct experiment; FD: conduct experiment. All authors read and approved the final manuscript.

371 **Funding** This work was supported by the National Natural Science Foundation of China (51104060,
372 51034006), Key Scientific Research Projects of Colleges and Universities of Henan Province
373 Education Department (21A440004), Taihang scholar program of Henan Polytechnic University for
374 2015, Jiangyin Science and Technology Innovation Special Fund project (JY0602A011002200024PB).

375 **Data availability** Not applicable.

376 **Compliance with ethical standards**

377 **Ethical approval** Not applicable

378 **Consent to participate** Not applicable

379 **Consent to publish** Not applicable

380 **Competing interest** The authors declare that they have no competing interest.

381 **References**

- 382 Costa FR, Leuteritz A, Wagenknecht U, Auf der Landwehr M, Jehnichen D, Haeussler L, Heinrich G
383 (2009) Alkyl sulfonate modified LDH: Effect of alkyl chain length on intercalation behavior,
384 particle morphology and thermal stability *Applied Clay Science* 44:7-14
385 doi:10.1016/j.clay.2008.12.020
- 386 Darmograi G, Prelot B, Layrac G, Tichit D, Martin-Gassin G, Salles F, Zajac J (2015) Study of
387 Adsorption and Intercalation of Orange-Type Dyes into Mg–Al Layered Double Hydroxide
388 *The Journal of Physical Chemistry C* 119:23388-23397 doi:10.1021/acs.jpcc.5b05510
- 389 Dinari M, Momeni MM, Ghayeb Y (2016) Photodegradation of organic dye by ZnCrLa-layered double
390 hydroxide as visible-light photocatalysts *Journal of Materials Science: Materials in Electronics*
391 27:9861-9869 doi:10.1007/s10854-016-5054-8
- 392 El Khanchaoui A, Sajieddine M, Mansori M, Essoumhi A Anionic dye adsorption on ZnAl
393 hydrotalcite-type and regeneration studies based on "memory effect" *Int J Environ Anal*
394 *Chem*:19 doi:10.1080/03067319.2020.1772769
- 395 Gao J et al. (2018) Efficient Removal of Methyl Orange and Heavy Metal Ion from Aqueous Solution
396 by NiFe-Cl-Layered Double Hydroxide *Environmental Engineering Science* 35:373-381
397 doi:10.1089/ees.2017.0023
- 398 Géraud E, Bouhent M, Derriche Z, Leroux F, Prévot V, Forano C (2007) Texture effect of layered
399 double hydroxides on chemisorption of Orange II *Journal of Physics and Chemistry of Solids*
400 68:818-823 doi:10.1016/j.jpcs.2007.02.053
- 401 Guo X, Yin P, Yang H (2018) Superb adsorption of organic dyes from aqueous solution on
402 hierarchically porous composites constructed by ZnAl-LDH/Al(OH)₃ nanosheets
403 *Microporous and Mesoporous Materials* 259:123-133 doi:10.1016/j.micromeso.2017.10.003
- 404 Jing C et al. (2019) Low Carbonate Contaminative and Ultrasmall NiAl LDH Prepared by Acid Salt
405 Treatment with High Adsorption Capacity of Methyl Orange *Industrial & Engineering*
406 *Chemistry Research* 58:11985-11998 doi:10.1021/acs.iecr.9b01706
- 407 Kausar A, Iqbal M, Javed A, Aftab K, Nazli Z-i-H, Bhatti HN, Nouren S (2018) Dyes adsorption using
408 clay and modified clay: A review *Journal of Molecular Liquids* 256:395-407
409 doi:10.1016/j.molliq.2018.02.034
- 410 Klopogge JT, Hickey L, Frost RL (2004) The effects of synthesis pH and hydrothermal treatment on
411 the formation of zinc aluminum hydrotalcites *Journal of Solid State Chemistry* 177:4047-4057
412 doi:10.1016/j.jssc.2004.07.010
- 413 Klopogge JT, Hickey L, Frost RL (2005) The effect of varying synthesis conditions on zinc chromium
414 hydrotalcite: a spectroscopic study *Materials Chemistry and Physics* 89:99-109
415 doi:10.1016/j.matchemphys.2004.08.035
- 416 Lei C, Zhu X, Zhu B, Jiang C, Le Y, Yu J (2017) Superb adsorption capacity of hierarchical calcined
417 Ni/Mg/Al layered double hydroxides for Congo red and Cr(VI) ions *J Hazard Mater*
418 321:801-811 doi:10.1016/j.jhazmat.2016.09.070
- 419 Li AY, Deng H, Ye CH, Jiang YH (2020) Fabrication and Characterization of Novel ZnAl-Layered

420 Double Hydroxide for the Superadsorption of Organic Contaminants from Wastewater ACS
421 Omega 5:15152-15161 doi:10.1021/acsomega.0c01092

422 Ling F, Fang L, Lu Y, Gao J, Wu F, Zhou M, Hu B (2016) A novel CoFe layered double hydroxides
423 adsorbent: High adsorption amount for methyl orange dye and fast removal of Cr(VI)
424 Microporous and Mesoporous Materials 234:230-238 doi:10.1016/j.micromeso.2016.07.015

425 Liu S-T, Huang J, Ye Y, Zhang A-B, Pan L, Chen X-G (2013) Microwave enhanced Fenton process for
426 the removal of methylene blue from aqueous solution Chemical Engineering Journal
427 215-216:586-590 doi:10.1016/j.cej.2012.11.003

428 Liu T, Jing L, Cui L, Liu Q, Zhang X (2018) Facile one-pot synthesis of a porphyrin-based hydrophilic
429 porous organic polymer and application as recyclable absorbent for selective separation of
430 methylene blue Chemosphere 212:1038-1046 doi:10.1016/j.chemosphere.2018.08.122

431 Liu X, Wang J (2021) Adsorptive removal of Sr(2+) and Cs(+) from aqueous solution by capacitive
432 deionization Environ Sci Pollut Res Int 28:3182-3195 doi:10.1007/s11356-020-10691-6

433 Mahjoubi FZ, Khalidi A, Abdennouri M, Barka N (2018) Zn–Al layered double hydroxides intercalated
434 with carbonate, nitrate, chloride and sulphate ions: Synthesis, characterisation and dye
435 removal properties Journal of Taibah University for Science 11:90-100
436 doi:10.1016/j.jtusc.2015.10.007

437 Mandal S, Kalaivanan S, Mandal AB (2019) Polyethylene Glycol-Modified Layered Double
438 Hydroxides: Synthesis, Characterization, and Study on Adsorption Characteristics for
439 Removal of Acid Orange II from Aqueous Solution ACS Omega 4:3745-3754
440 doi:10.1021/acsomega.8b02743

441 Mandal S, Tichit D, Lerner DA, Marcotte N (2009) Azoic Dye Hosted in Layered Double Hydroxide:
442 Physicochemical Characterization of the Intercalated Materials Langmuir 25:10980-10986
443 doi:10.1021/la901201s

444 Maneerung T, Liew J, Dai Y, Kawi S, Chong C, Wang CH (2016) Activated carbon derived from
445 carbon residue from biomass gasification and its application for dye adsorption: Kinetics,
446 isotherms and thermodynamic studies Bioresour Technol 200:350-359
447 doi:10.1016/j.biortech.2015.10.047

448 Mohapatra L, Parida KM (2012) Zn–Cr layered double hydroxide: Visible light responsive
449 photocatalyst for photocatalytic degradation of organic pollutants Separation and Purification
450 Technology 91:73-80 doi:10.1016/j.seppur.2011.10.028

451 Morshedi D, Mohammadi Z, Akbar Boojari MM, Aliakbari F (2013) Using protein nanofibrils to
452 remove azo dyes from aqueous solution by the coagulation process Colloids Surf B
453 Biointerfaces 112:245-254 doi:10.1016/j.colsurfb.2013.08.004

454 Mustapha Bouhent M, Derriche Z, Denoyel R, Prevot V, Forano C (2011) Thermodynamical and
455 structural insights of orange II adsorption by MgRAINO₃ layered double hydroxides Journal
456 of Solid State Chemistry 184:1016-1024 doi:10.1016/j.jssc.2011.03.018

457 Ou W, Zhang G, Yuan X, Su P (2015) Experimental study on coupling photocatalytic oxidation process
458 and membrane separation for the reuse of dye wastewater Journal of Water Process
459 Engineering 6:120-128 doi:10.1016/j.jwpe.2015.04.001

460 Pakshirajan K, Kheria S (2012) Continuous treatment of coloured industry wastewater using
461 immobilized Phanerochaete chrysosporium in a rotating biological contactor reactor J Environ
462 Manage 101:118-123 doi:10.1016/j.jenvman.2012.02.008

463 Parida K, Mohapatra L (2012) Recent progress in the development of carbonate-intercalated Zn/Cr

464 LDH as a novel photocatalyst for hydrogen evolution aimed at the utilization of solar light
465 Dalton Transactions 41:1173-1178 doi:10.1039/C1DT10957J

466 Rathee G, Singh N, Chandra R (2020) Simultaneous Elimination of Dyes and Antibiotic with a
467 Hydrothermally Generated NiAlTi Layered Double Hydroxide Adsorbent ACS Omega
468 5:2368-2377 doi:10.1021/acsomega.9b03785

469 Rojas Delgado R, Arandigoyen Vidaurre M, De Pauli CP, Ulibarri MA, Avena MJ (2004)
470 Surface-charging behavior of Zn-Cr layered double hydroxide J Colloid Interface Sci
471 280:431-441 doi:10.1016/j.jcis.2004.08.045

472 Sun Q, Chen B (2020) Biotemplated Fabrication of 3D Hierarchically Porous MgAl-LDH/CF
473 Composites with Effective Adsorption of Organic Dyes from Wastewater Industrial &
474 Engineering Chemistry Research 59:16838-16850 doi:10.1021/acs.iecr.0c02800

475 Sun Q, Tang M, Hendriksen PV, Chen B (2020) Biotemplated fabrication of a 3D hierarchical structure
476 of magnetic ZnFe₂O₄/MgAl-LDH for efficient elimination of dye from water Journal of
477 Alloys and Compounds 829 doi:10.1016/j.jallcom.2020.154552

478 Tao X, Liu D, Song J, Ye Q, Xu D (2017) Plasma modification of ZnMgAl-LDHs for adsorption
479 property improvement Journal of the Taiwan Institute of Chemical Engineers 74:281-288
480 doi:10.1016/j.jtice.2017.02.009

481 Taviot-Guého C, Prévot V, Forano C, Renaudin G, Mousty C, Leroux F (2018) Tailoring Hybrid
482 Layered Double Hydroxides for the Development of Innovative Applications Advanced
483 Functional Materials 28:1703868 doi:10.1002/adfm.201703868

484 X. Ruan, Huang S, H. Chen, Qian G (2013) Sorption of aqueous organic contaminants onto dodecyl
485 sulfate intercalated magnesium iron layered double hydroxide Applied Clay Science
486 72:96-103 doi:10.1016/j.clay.2013.01.001

487 Xu J, Deng H, Song J, Zhao J, Zhang L, Hou W (2017) Synthesis of hierarchical flower-like Mg₂Al-Cl
488 layered double hydroxide in a surfactant-free reverse microemulsion J Colloid Interface Sci
489 505:816-823 doi:10.1016/j.jcis.2017.06.080

490 Yan Z, Zhu B, Yu J, Xu Z (2016) Effect of calcination on adsorption performance of Mg-Al layered
491 double hydroxide prepared by a water-in-oil microemulsion method Rsc Advances
492 6:50128-50137 doi:10.1039/c6ra05253c

493 Zhang P, Ouyang S, Li P, Huang Y, Frost RL (2019a) Enhanced removal of ionic dyes by hierarchical
494 organic three-dimensional layered double hydroxide prepared via soft-template synthesis with
495 mechanism study Chemical Engineering Journal 360:1137-1149 doi:10.1016/j.cej.2018.10.179

496 Zhang Q, Zhang YD, Chen JT, Liu QF (2019b) Hierarchical Structure Kaolinite Nanospheres with
497 Remarkably Enhanced Adsorption Properties for Methylene Blue Nanoscale Research Letters
498 14 doi:10.1186/s11671-019-2934-x

499 Zheng Y-M, Li N, Zhang W-D (2012) Preparation of nanostructured microspheres of Zn-Mg-Al
500 layered double hydroxides with high adsorption property Colloids and Surfaces A:
501 Physicochemical and Engineering Aspects 415:195-201 doi:10.1016/j.colsurfa.2012.10.014

502 Zheng Y, Cheng B, You W, Yu J, Ho W (2019) 3D hierarchical graphene oxide-NiFe LDH composite
503 with enhanced adsorption affinity to Congo red, methyl orange and Cr(VI) ions J Hazard
504 Mater 369:214-225 doi:10.1016/j.jhazmat.2019.02.013

505 Zheng Y, Zhu B, Chen H, You W, Jiang C, Yu J (2017) Hierarchical flower-like nickel(II) oxide
506 microspheres with high adsorption capacity of Congo red in water J Colloid Interface Sci
507 504:688-696 doi:10.1016/j.jcis.2017.06.014

508 Zubair M, Jarrah N, Ihsanullah, Khalid A, Manzar MS, Kazeem TS, Al-Harhi MA (2018)
509 Starch-NiFe-layered double hydroxide composites: Efficient removal of methyl orange from
510 aqueous phase Journal of Molecular Liquids 249:254-264 doi:10.1016/j.molliq.2017.11.022
511

Figures

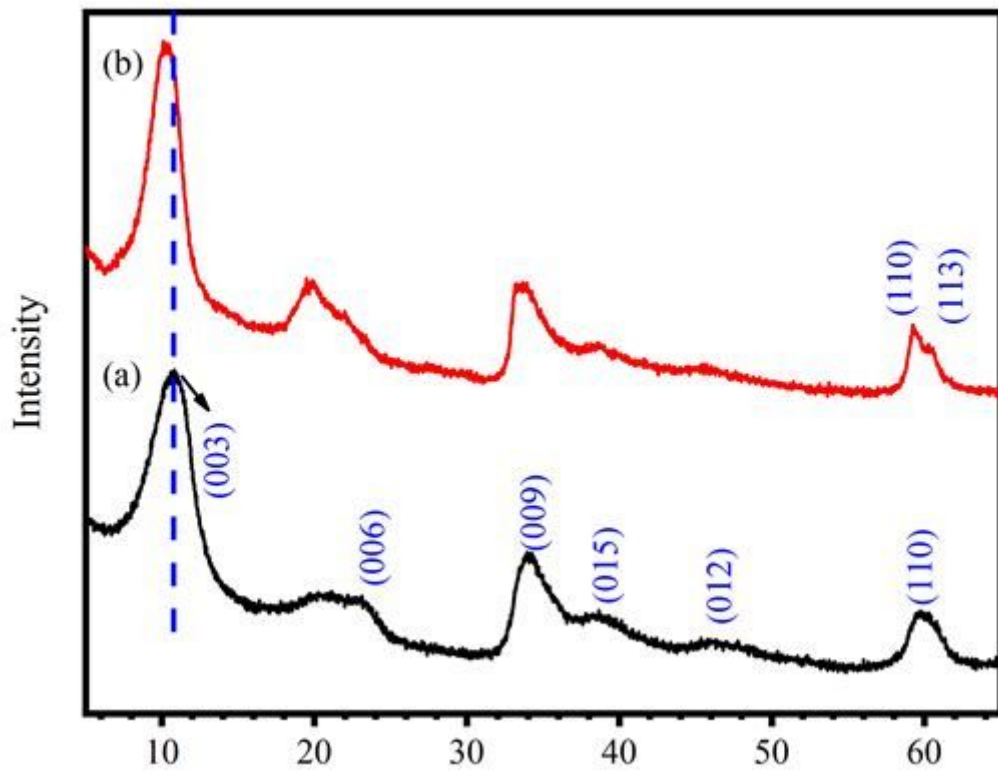


Figure 1

XRD patterns for the (a) NO₃-LDH and (b) SO₃-LDH

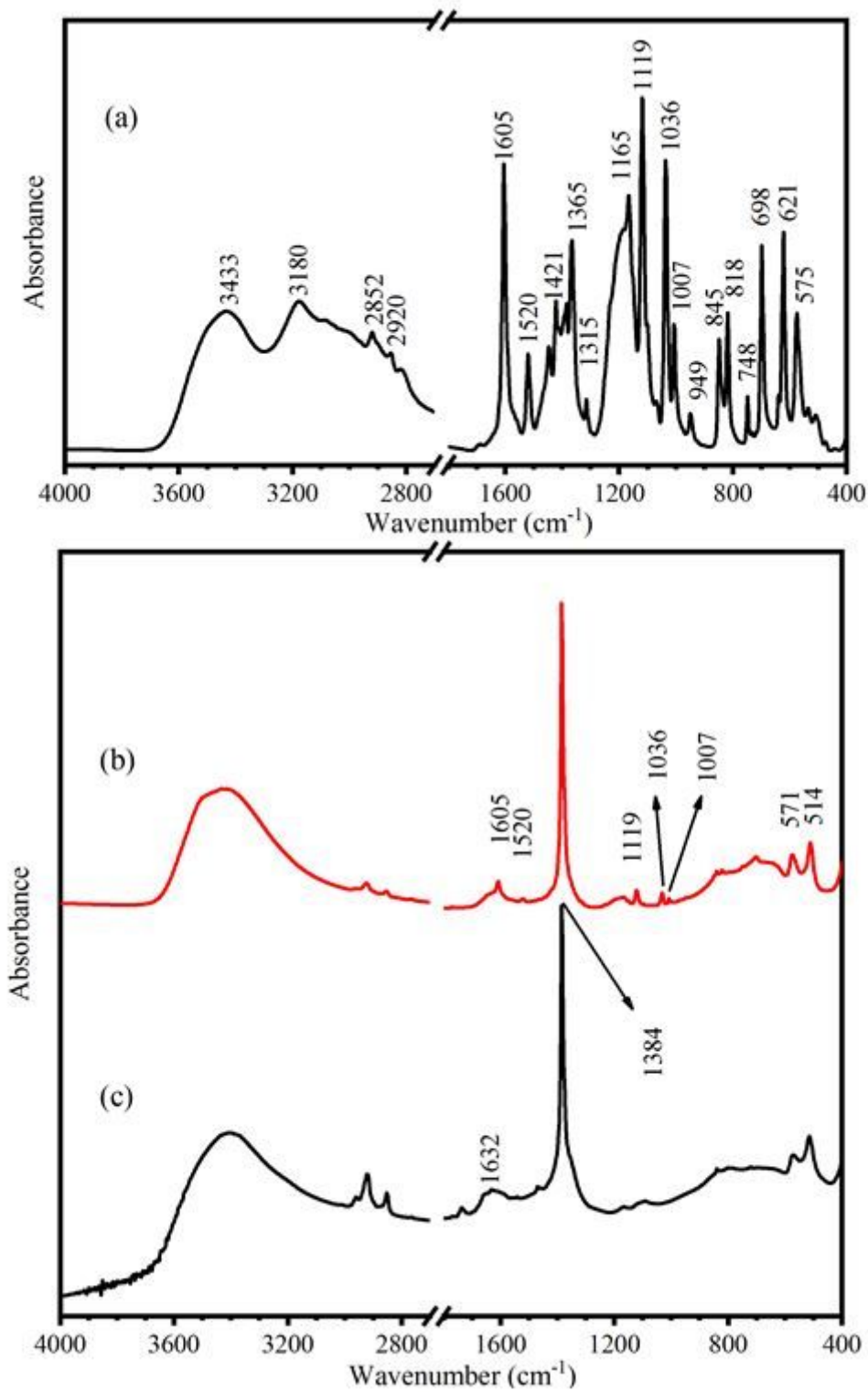


Figure 2

FT-IR spectra for (a) Modifier, (b) $\text{SO}_3\text{-LDH}$ and (c) $\text{NO}_3\text{-LDH}$

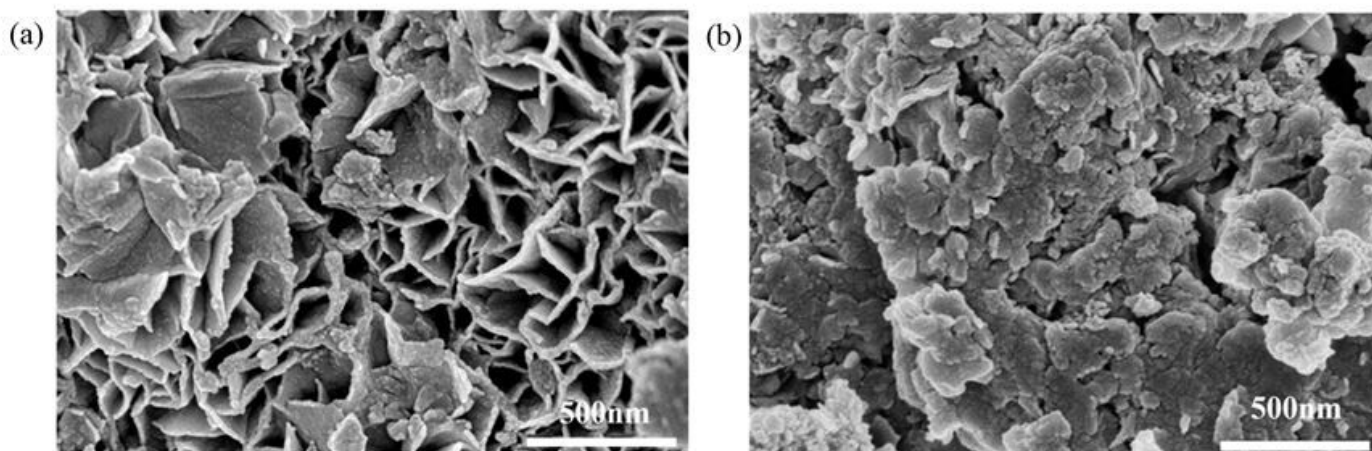


Figure 3

SEM images of (a) NO₃-LDH and (b) SO₃-LDH

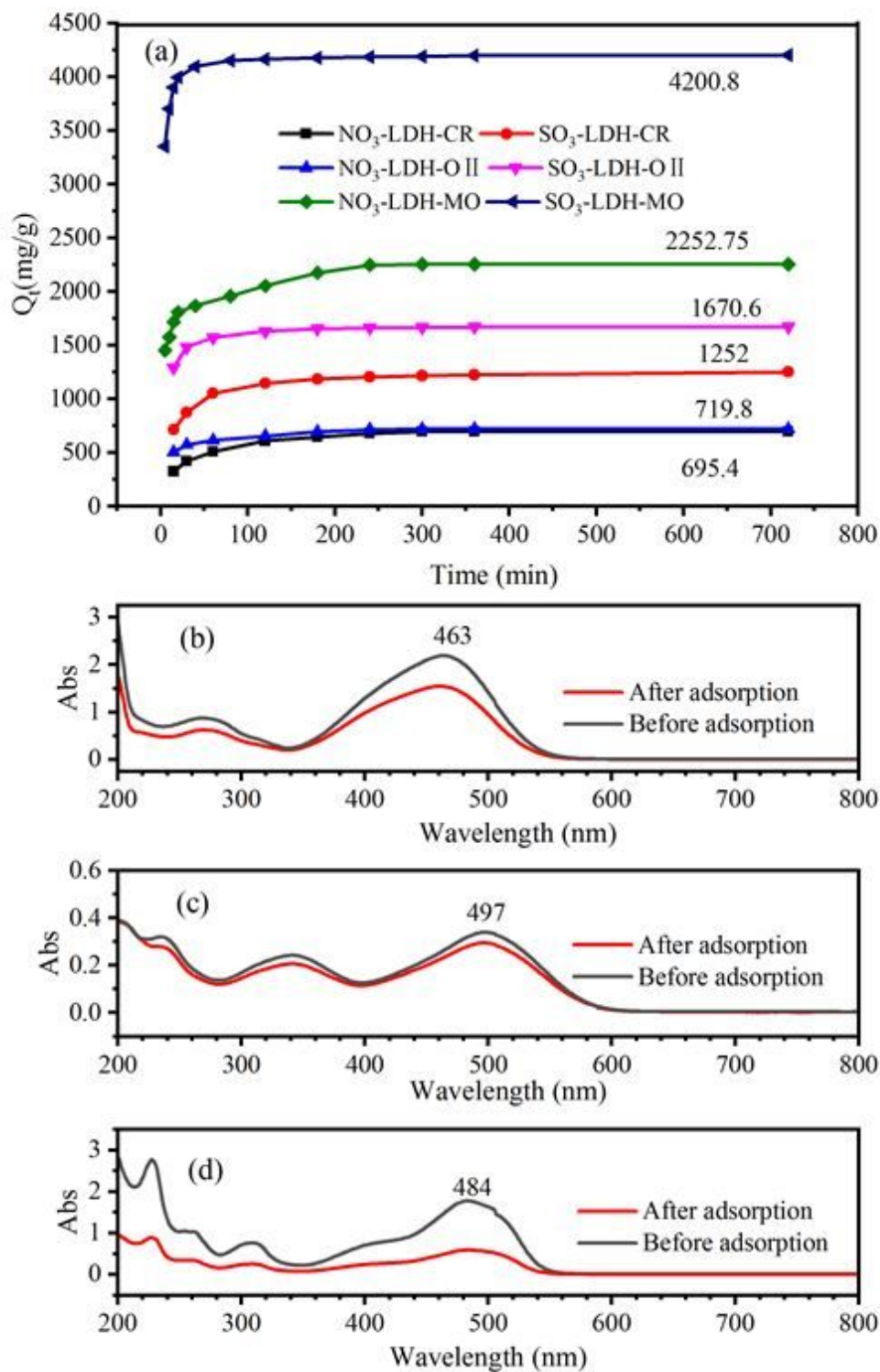


Figure 4

Adsorption of dyes by NO₃-LDHs and SO₃-LDH (a) ; Spectral scanning curve of (b) MO, (c) CR and (d) OII before and after SO₃-LDH adsorption

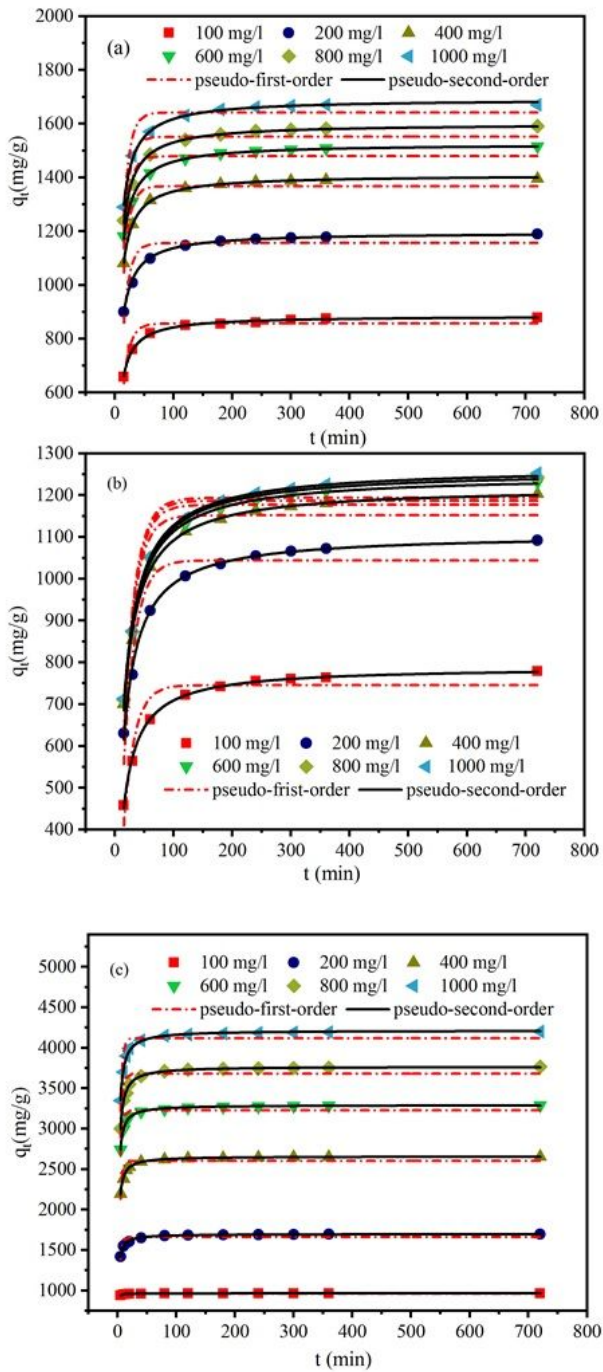


Figure 5

Fitted plots of the pseudo-first-order and pseudo-second-order kinetic models for (a) OII, (b) CR and (c) MO adsorption by S03-LDH

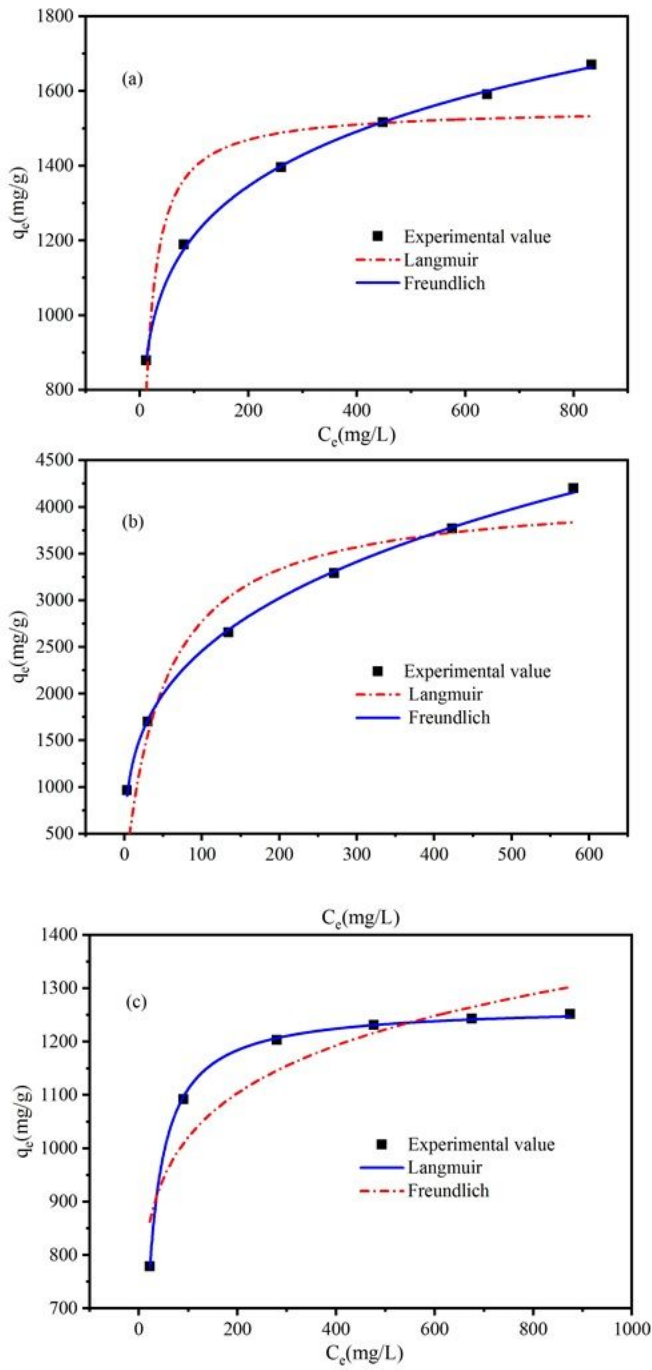


Figure 6

Isotherm model for (a) Oil, (b) MO and (c) CR adsorption on SO₃-LDH

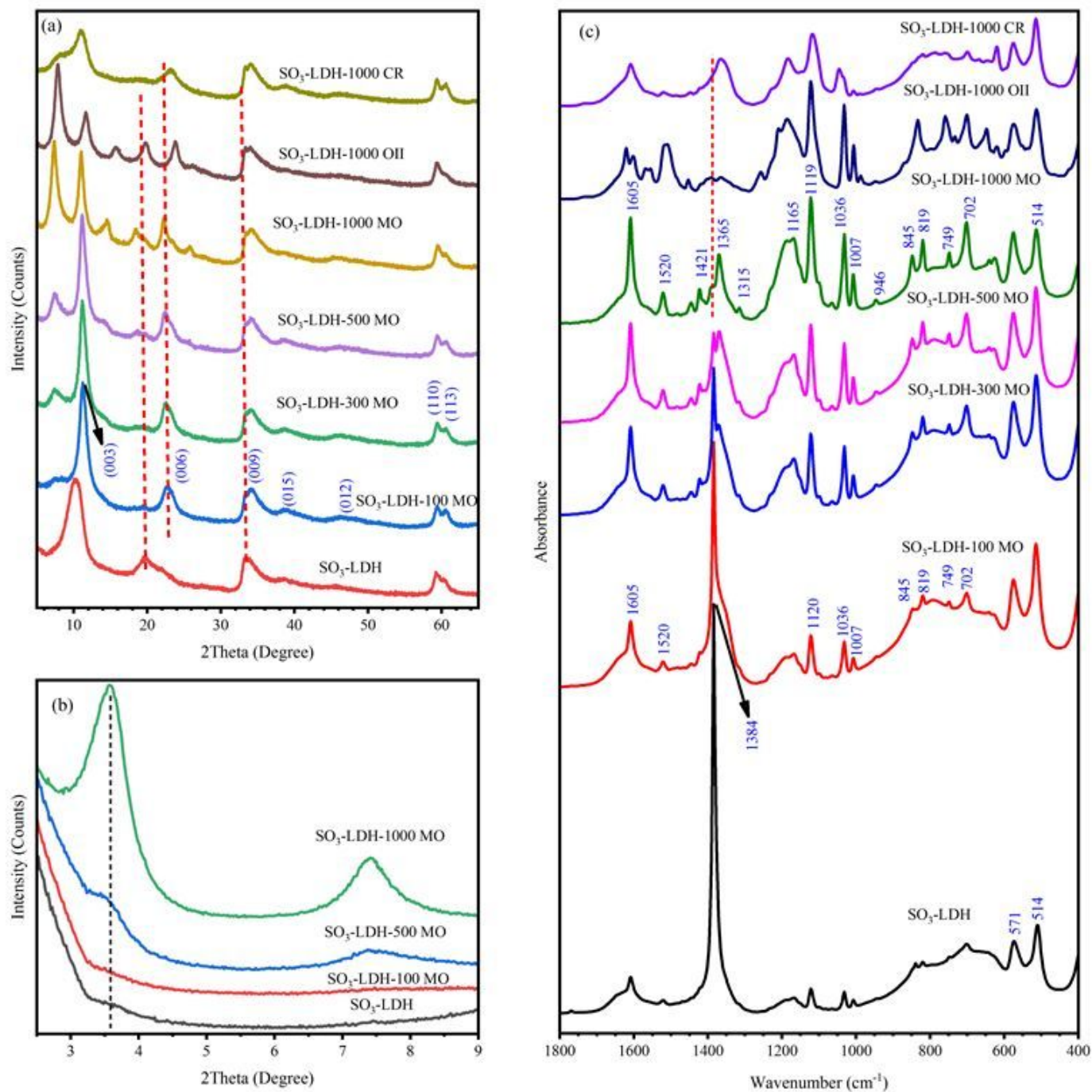


Figure 7

The XRD patterns (a, b) and FTIR spectra (c) of different dyes adsorbed by $\text{SO}_3\text{-LDH}$

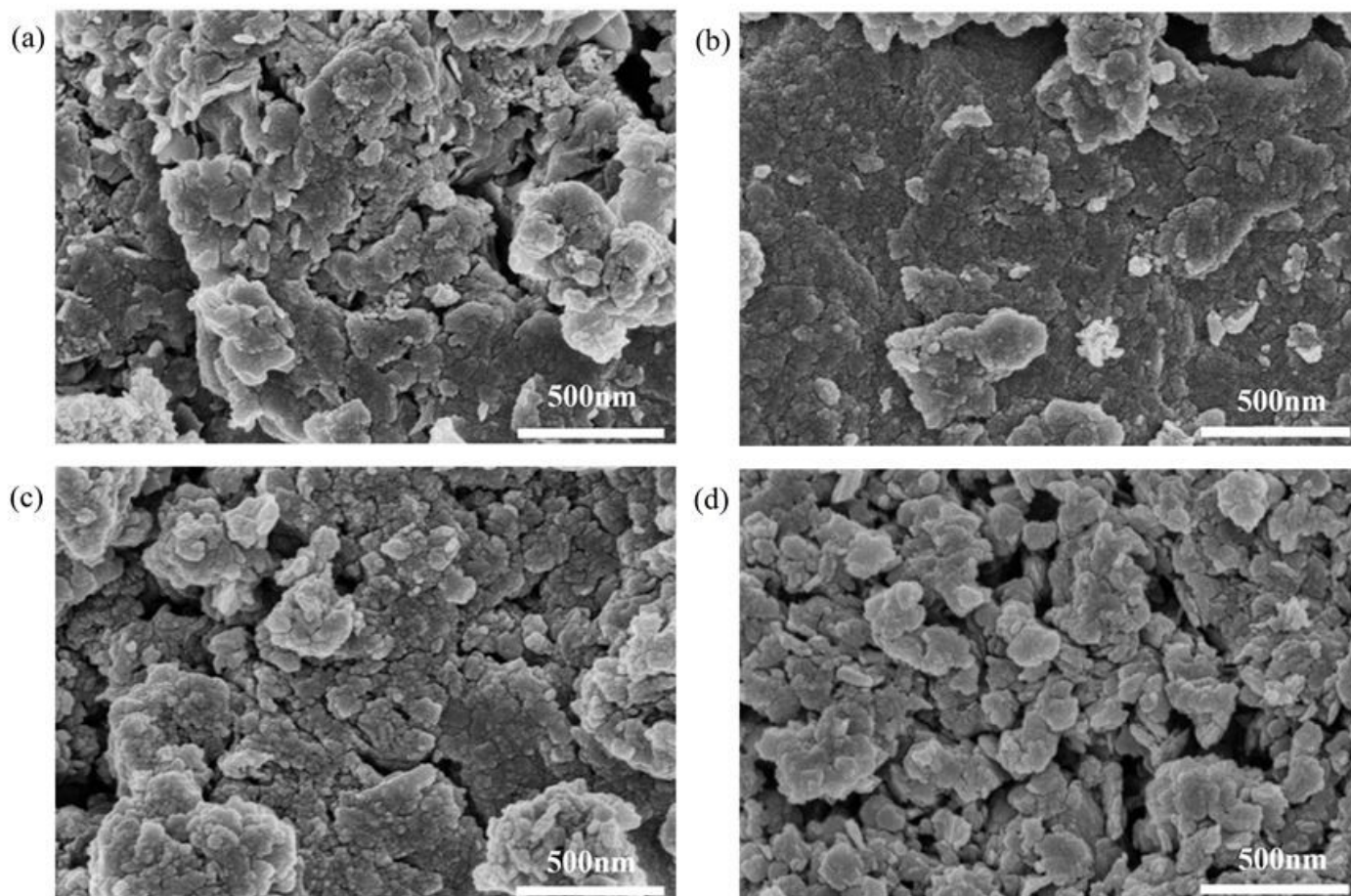


Figure 8

SEM images of SO₃-LDH before and after adsorbed different concentrations MO solutions: (a) 0 mg/L, (b) 100 mg/L, (c) 500 mg/L and (d) 1000 mg/L

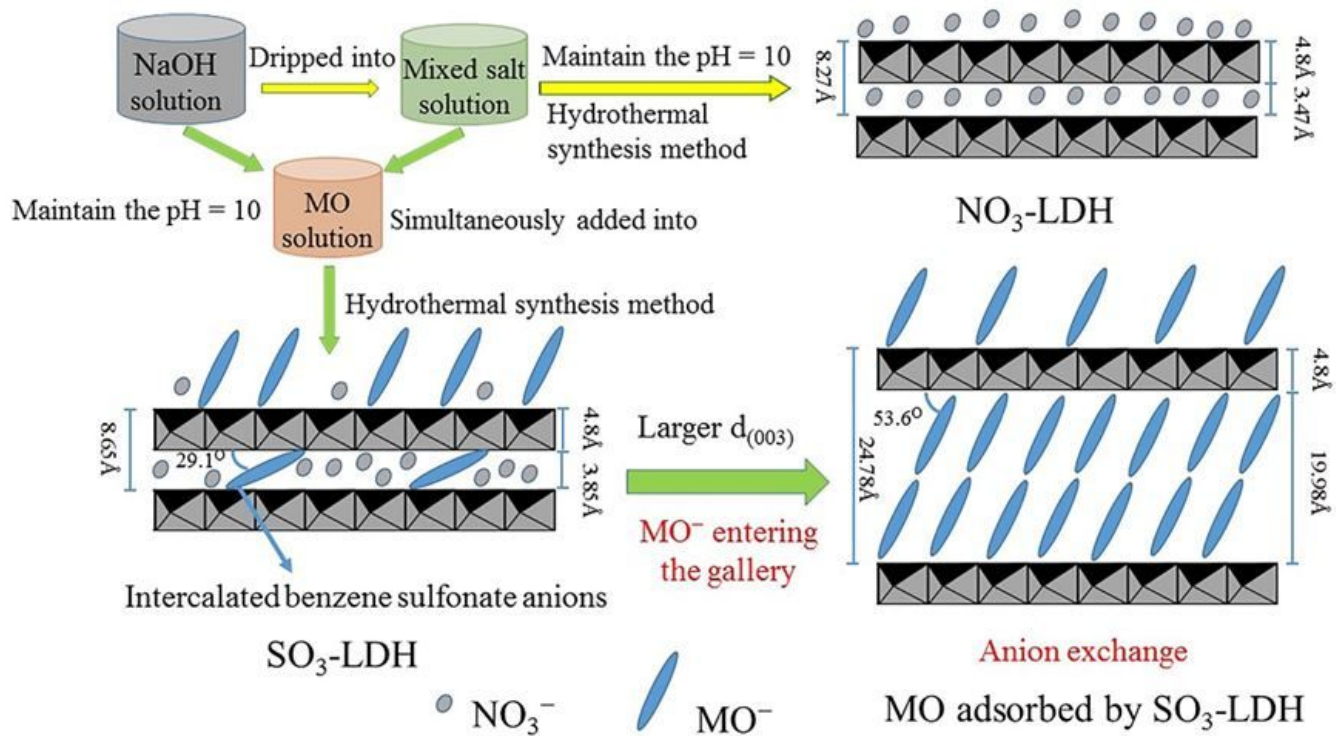


Figure 9

Schematic illustration of the synthetic process of LDH materials and adsorption process of MO by SO₃-LDH

Supplementary Files

This is a list of supplementary files associated with this preprint. Click to download.

- [GraphicalAbstract.doc](#)